Rev. Roum. Sci. Techn.– Électrotechn. et Énerg.
Vol. **69**, *1*, pp. 15–20, Bucarest, 2024

MAXIMUM POWER POINT TRACKING IN A PEROVSKITE SOLAR PUMPING SYSTEM WITH A SIX-PHASE INDUCTION MOTOR

MOHAMED I. ABDELWANIS[1], ALAA A. ZAKY[2]

Keywords: Renewable energy; Six-phase induction motor; Maximum power point tracking (MPPT); Genetic algorithm (GA); Perovskite solar cells.

In this work, the maximum power point (MPP) of a photovoltaic (PV) array utilized as a source of electricity in standalone mode is tracked using a genetic algorithm (GA) as an optimization tool. The major objective of this work is to implement and regulate a six-phase induction motor (SPIM) powered by a centrifugal pump and fed by a perovskite solar array through a three-phase inverter. Perovskite solar cells are the most promising third-generation photovoltaic technology to replace silicon-based photovoltaic. These cells are made cheaply, at a low temperature, and efficiently. The outcomes are then investigated utilizing a SPIM scaler (v/f) closed-loop control. PID controllers are tuned to keep the motor speed aligned with the reference value. The transformer's six-phase secondary is linked to an LC filter to reduce the voltage and current waveform ripple. A test setup was created and installed to investigate the potential of controlling the SPIM fed via a three-to-six-phase transformer. The findings showed that the area needed for the plates when utilizing perovskite solar cells is just 14 % of what it would be if a silicon-based solar array were used for the identical purpose. Perovskite solar cells' tiny surface area helps to prevent partial shading and lower costs. It was discovered that the suggested method works well for powering SPIM from a three-phase source.

1. **INTRODUCTION**

The world's energy consumption is continually rising. Thus, new energy sources should be discovered, investigated, and developed to meet future consumption [1]. Photovoltaic (PV) energy appears to be the most hopeful renewable energy source, as it is available practically everywhere, in contrast to other forms such as geothermal, wind, waves, and biomass [2].

Due to a fast drop in the cost of PV modules, the pace of adoption of solar PV by industries and instant consumers is increasing. Furthermore, fossil fuel resources are depleting at an increasing rate, attracting even more attention to PV technology [3]. The technology above has various advantages, including surviving indefinitely, producing no pollution, and having no operating costs [4]. It's being used in a variety of applications, including water pumping. Solar PV-based water pumping has recently been concentrated on for human and industrial consumption [5].

Perovskite absorbers have been utilized extensively in solar cells due to their optoelectronic properties, which include a configurable band gap, high carrier mobility, and long carrier lifetime [6,7]. The perovskite solar cell transformation efficiency depends on perovskite as the absorber layer is increasing rapidly [8,9], reaching more than 25 % recently, overcoming other counterpart third-generation photovoltaic [10]. Perovskite solar cells have a planar structure and a mesoporous one. The main drawbacks of this type of solar cell are the hysteresis phenomenon and the stability problem of perovskite [11]. Interface engineering approaches are suitable solutions for overcoming hysteresis and stability problems and increasing power conversion efficiency [12].

Because of its low cost, improving the MPPT technique is the simplest element to implement, and it may be employed even in existing equipment by upgrading the control algorithms [13]. Significant development has been achieved in MPPT techniques over the previous few decades, and these methods are classified as offline, online, and mixed methods [14].

Because of their advantages over typical three-phase drives, multiphase drives have piqued the interest of the power electronics, control, machines, and driving communities [1]. A six-phase IM for industrial applications has several advantages over a three-phase system, including increased dependability, reduced magnetic flux harmonics, reduced torque pulsations, and lower static converter power ratings [15]. Due to these factors, six-phase IM is becoming popular in high-power applications.

For the constant and variable speed applications, this research provides a drive system for the modified six-phase IM. The traditional three-phase inverter is coupled to three single-phase primary and two secondary transformers in variable-speed applications. A three-to-six-phase transformer feeds the redesigned six-phase motor [16]. The redesigned six-phase motor's speed is controlled using the scalar v/f closed-loop technique. When a three-to-six-phase transformer is sufficient for constant speed applications.

The following is the structure of this paper: The introduction and literature review are all included in section 1. The modeling of perovskite solar cells is shown in section 2. The modeling of the boost converter is shown in section 3. The explanation of the genetic algorithm is presented in section 4. The modeling of the improved six-phase IM is presented in section 4. The six-phase inverter modeling is presented in section 5. The modeling of three to six-phase transformers is presented in section 6. The modeling of the six-phase induction motor is shown in section 7. The control strategy is presented in section 8. Section 9 shows how to run a six-phase IM process using a perovskite solar array and a GA-fed six-phase variable speed drive to feed an MPPT-controlled boost converter. Finally, section 10 summarizes the outcomes of this study's findings.

2. **MODELLING OF PEROVSKITE SOLAR CELLS**

Perovskite solar cells are fabricated in this work as follows; Fluorine-doped tin oxide (FTO) conductive glasses sonicated via sonication bath each 15 minutes in the order of Hellmanex, 2-propanol, and acetone for cleaning. Electron transporting layer (ETL) which is also called titania layer was spin coated over the cleaned FTO glasses after 15 minutes UV ozone treatment. The ETL consisting of titanium (IV) isopropoxide solution dissolved in ethanol and spin coated at 2 000 rpm for 60 s and then annealing for 45 minutes at 500ºC in oven at 5 °C/min as a temperature ramp rate. The perovskite layer which is the active layer where the light produces pairs of hole-electrons and hole-

[1,2] Electrical Engineering Department, Kafrelsheikh University, Kafrelsheikh 33511, Egypt
E-mails: mohamed.soliman4@eng.kfs.edu.eg, alaa.hussien@eng.kfs.edu.eg

DOI: 10.59277/RRST-EE.2024.69.1.3

transporting layer (HTL) were prepared inside glove box which is argon-filled. The perovskite 40 wt. % solutions formed from methyl ammonium iodide and lead acetate trihydrate in anhydrous DMF with a molar ratio of 3:1 and finally a hypo phosphorous acid 10µl/ml was added to the solution. The films then left for 10 minutes at the room temperature to dry following by annealing for 5 minutes at 100 °C.

As depicted in Fig. 1, a solar PV water pumping system consists of a motor, pumping set, boost converter, PWM inverter, and PV array. The following is a list of the individual parts and their descriptions:

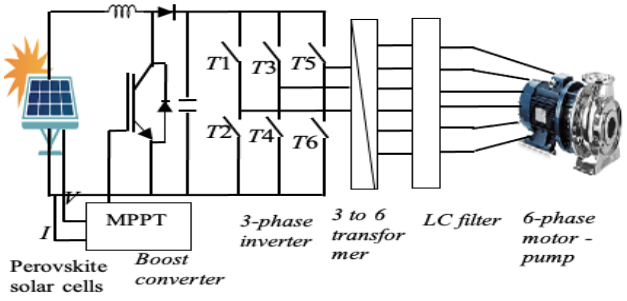

Fig. 1 – Block diagram of perovskite solar cells pumping system.

PV array modelling can be done with either single or double diode equations. The ideality factor is assumed to be constant in the single diode [17]. The ideality factor is a function of the voltage across the device. When the device's recombination is dominated by the surfaces and bulk areas at high voltage, the ideality factor is closes to one. At lower voltages, however, recombination in the junction takes over, and the ideality factor terms to two where its value can reach till 5 in the perovskite solar cells due to the perovskite material behavior. Figure 2 depicts a PV array with two diodes. The PV output current I_{pv} in this model is calculated as follows:

$$I_{pv} = I_{ph} + I_{D1} + I_{D2} + I_{sh}\,, \tag{1}$$

where: I_{ph} is the source input current, I_{D1}, I_{D2} are the two diodes' currents, I_{sh} is the shunt current, V_{pv} is the PV output voltage, and R_{sh} is the shunt resistance.

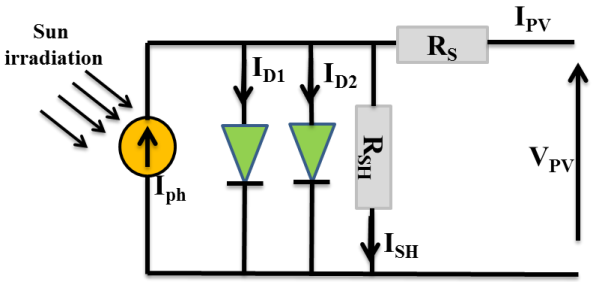

Fig. 2- Circuit diagram of the double diodes model.

The PV current $I_{ph,}$ I_{D1}, I_{D2} , and I_{sh} are computed as:

$$I_{ph} = (I_{sn} + k\Delta T)\frac{G}{G_n}\,, \tag{2}$$

$$I_{D1} = I_o\left[e^{\frac{q(V_{pv}+I_{pv}R_S)}{m_1 kT}}\right], \tag{3}$$

$$I_{D2} = I_o\left[e^{\frac{q(V_{pv}+I_{pv}R_S)}{m_2 kT}}\right], \tag{4}$$

$$I_{sh} = \frac{V_{pv}+I_{pv}R_S}{R_{sh}}\,, \tag{5}$$

where G is the solar radiation, G_n is the solar rated radiation, m_1 and m_2 are the diode ideality factor of 1 and 2.

3. BOOST CONVERTER MODELING

The boost converter, which is a high-efficiency step-up dc/dc switching converter, is the second element. For an inductor voltage pulse width modulation, the converter uses a transistor switch, commonly a MOSFET [18]. A triangular current waveform is produced by rectangular voltage pulses into an inductor. The following assumptions were made in this study: the boost converter is run in continuous mode, which means that the current of the inductor never falls to zero. The boost converter's circuit diagram is shown in Fig. 3 [3]:

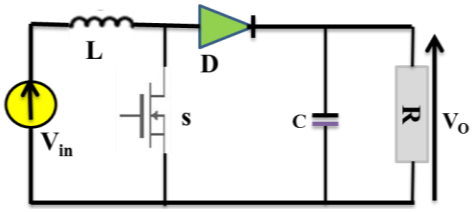

Fig. 3 – Circuit diagram of the boost converter.

The diode voltage drop is V_D, while the transistor voltage drop is V_{Trans}. The output voltage V_o in term of V_{in} can be calculated from:

$$V_o = \frac{V_{in}-V_{Trans}D}{1-D} - V_D\,. \tag{6}$$

Solving the previous equation for the duty cycle, D is:

$$D = \frac{V_o-V_{in}+V_D}{V_o+V_D-V_{Trans}}\,. \tag{7}$$

Neglecting both the voltage drops through the diode and transistor then the V_o is:

$$V_o = \frac{V_{in}}{1-D}\,. \tag{8}$$

The inductor L is kept in continuous mode when this criterion is met. This can be expressed as follows [19]:

$$L = \frac{(V_o-V_{in}+V_D)(1-D)}{\min(i_{load})f}\,. \tag{9}$$

Under specific operating circumstances, the (MPPT) algorithm is combined with genetic algorithms (GA) to extract the most power possible from the PV modules [20]. This is done by measuring and adjusting the DC current and voltage by adjusting the duty cycle D of the boost chopper. Solar radiation, ambient temperature, and solar cell temperature all affect maximum power]21,22[. When the operational voltage of a PV panel is perturbed by a minor deviation, if the resulting change in power P is positive, the direction will go to MPP and continue perturbing in the same direction, according to the MPPT algorithm. If P is negative, the direction of the perturbation will be far from the MPP, and the sign of the perturbation must be modified [23].

4. GENETIC ALGORITHM

The genetics algorithm GA is a search tool inspired by biology; the goal is to leverage reproduction and natural selection concepts in computing to solve search problems. Figure 4 shows the Flow chart of MPPT of perovskite solar cells. The following is a summary of the GA [13]:

1. Create a random population of N chromosomes to begin (suitable solutions for the MPPT)
2. Fitness: Evaluate each chromosome x in the population's fitness (or cost function) $f(x)$.
3. Create a new population by repeating the previous procedures until the new population is complete.

• Selection: From a population, choose two parent chromosomes based on their fitness (the better fitness, the bigger chance to be selected)

• Crossover: With a crossover chance, the parents will cross over to produce new offspring (children). If no crossover occurs, the offspring is a carbon duplicate of the parents.

• Mutation: Create new offspring at each locus with a mutation probability (position in chromosome).

• Accepting: Add new members to the population.

4. Replace: For a second run of the algorithm, use the newly crea ted population.

5. Stop and return the best solution in the current population if the end condition is satisfied

6. Return to step 2 of the loop.

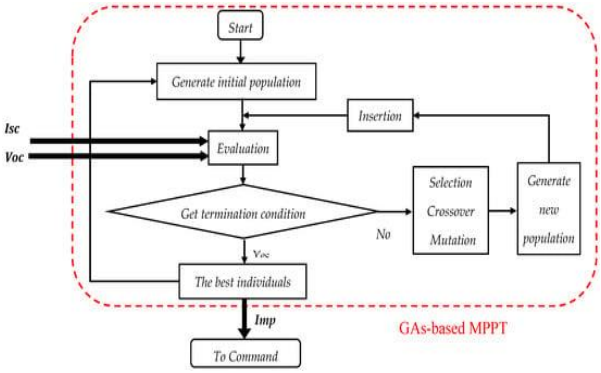

Fig. 4 – Flow chart of MPPT of perovskite solar cells-based GA.

5. MODELING OF THREE-PHASE INVERTER

By altering the *v*/*f* ratio to manage the speed of the induction motor, a three-phase inverter with a suitable pulse width modulation (PWM) method can create a sinusoidal waveform. Figure 5 depicts the three-phase PWM inverter's circuit. The Kirchhoff voltage law equation of Fig. 5 is presented as [24]

$$\begin{bmatrix} v_{an} \\ v_{bn} \\ v_{cn} \end{bmatrix} = \frac{1}{3}\begin{bmatrix} 2 & -1 & -1 \\ 1 & 2 & -1 \\ 1 & 1 & 2 \end{bmatrix}\begin{bmatrix} v_{ao} \\ v_{bo} \\ v_{co} \end{bmatrix}. \tag{10}$$

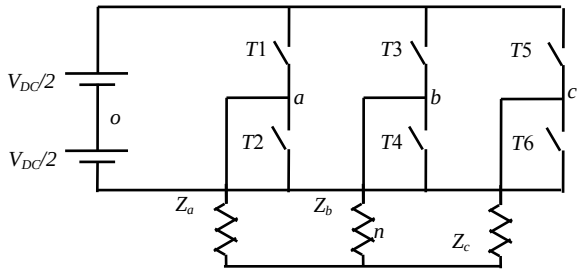

Fig. 5 – Schematic diagram of three phase inverter.

6. THREE TO SIX PHASE TRANSFORMER

The primary and secondary windings are coupled in Figure 6 to create a three-phase star in primary and a six-phase star in secondary [25].

Using specified turn ratios, the balanced output phase voltage (with 60° phase angles between each phase) is calculated. The input–output relationship is given by the eq. [25]: the letters A, B, and C stand for the three-phase side, while the letters a, b, c, d, e, and f stand for the six-phase side. The mathematical underpinning for this connection is the fundamental sum of the waveform's magnitude and angle:

$$\begin{bmatrix} V_a \\ V_b \\ V_c \\ V_d \\ V_e \\ V_f \end{bmatrix} = \begin{bmatrix} 1 & 0 & 0 \\ 0 & 0 & -1 \\ 0 & 1 & 0 \\ -1 & 0 & 0 \\ 0 & 0 & 1 \\ 0 & -1 & 0 \end{bmatrix}\begin{bmatrix} V_A \\ V_B \\ V_C \end{bmatrix}. \tag{11}$$

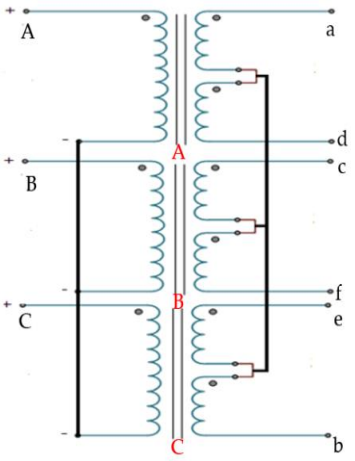

Fig. 6 – Schematic diagram of three-to-six phase transformer connection.

7. MODELING OF MULTI-PHASE IM

The winding of a six-phase IM is made up of two 3-phase IM, which has been displaced by 60 degree electrostatic [26].

The V_d, V_q component of the voltage *d*-*q* axis can be computed as [27],

$$V_q = \frac{2}{6}\left[\sum_{k=1}^{6} v_k \sin\left(\theta - \frac{(k-1)\pi}{6}\right)\right], \tag{12}$$

$$V_d = \frac{2}{6}\left[\sum_{k=1}^{6} v_k \sin\left(\theta - \frac{(k-1)\pi}{6}\right)\right]. \tag{13}$$

The ψ_{qs}, ψ_{qr} component of the rotor flux q axis can be calculated from [30]:

$$\psi_{qs} = \frac{i}{s}\left[V_{qs} - \frac{R_s}{L_s}\left[\psi_{qs} - L_m i_{qr}\right] - \omega_e \psi_{ds}\right], \tag{14}$$

$$\psi_{qr} = \frac{i}{s}\left[-\frac{R_r}{L_r}\left[\psi_{qr} - L_m i_{qs}\right] + (\omega_r - \omega_e)\psi_{dr}\right], \tag{15}$$

where R_s denotes the resistance of the stator, and the rotor resistance is R_r. L_s, L_r, and L_m stator, rotor, and magnetizing inductances, respectively, i_{qr} current of rotor conductor on the *q*-axis, i_{qs} current of stator conductor on the *q*-axis. ψ_{dr}, ψ_{ds} rotor and stator *d*-axis fluxes are written as [28]:

$$\psi_{ds} = \frac{1}{s}\left[V_{ds} - \frac{R_s}{L_s}\left[\psi_{ds} - L_m i_{dr}\right] + \omega_e \psi_{qs}\right], \tag{16}$$

$$\psi_{dr} = \frac{1}{s}\left[\frac{R_r}{L_r}\left[\psi_{qr} - L_m i_{ds}\right] + (\omega_e - \omega_r)\psi_{qr}\right], \tag{17}$$

where i_{dr} ,i_{ds} *d*-axis rotor and stator currents.

The electrical torque T_e and rotating angular speed ω_r are computing from [24,29]:

$$T_e = \frac{6}{2}\frac{P}{2}\left[\psi_{ds} i_{qs} - \psi_{qs} i_{ds}\right], \tag{18}$$

$$\omega_r = \frac{p}{2}\frac{1}{s}\left[\frac{1}{J}\left(T_e - T_L - D\frac{2}{p}\omega_r\right)\right], \tag{19}$$

where *p* represents the six-phase IM poles, T_L represents the mechanical torque, *J* represents the motor moment of inertia, *D* represents the mechanical friction coefficient [30].

8. PROPOSED CONTROL METHOD

The closed loop (*v*/*f*) is the kind of speed control characterized by its high precision and eases of follow the desired speed. To keep the motor speed tracking the desired speed, the suggested PID controller approach is employed to

imitate a *v*/*f* control. The suggested scalar (*v*/*f*) system of a perovskite solar cells used to feed six-phase inverter supplied to a 6-phase IM is shown schematically in Fig. 7.

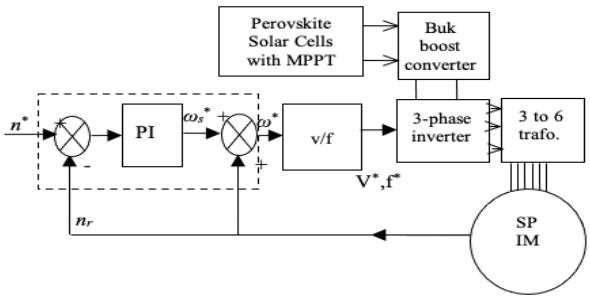

Fig. 7 – The block diagram of PID six-phase IM control.

The error between mechanical speed and desired speed generates the slip speed through the PID controller. The slip frequency ω* instruction is made by multiplying the rotor speed by the slip speed ω_s*. A *v*/*f* computation produces the voltage references from the slip frequency references. The slip speed ω* is raised, giving in a + error, and the slip s* is increased to its highest value. The slip frequency ω* increases, resulting in a positive mistake, and the slip speed ω_s* is set to its highest value. The motor accelerates at the highest drive current to decrease the speed error to a lowering, giving the most torque possible. The slip speed ω* is reduced, giving in a negative error, and the slip speed ω_s* is set to its highest negative value. The motor reduced the speed mistake to a minimum at the highest inverter current, producing the maximum pull-out torque possible. Finally, the motor drive maintains a slip where the motor and load torque are equal.

9. **SPIM SIMULATION AND IMPLEMENTATION**

9.1. EXPERIMENTAL SYSTEM

As shown in Fig. 8, the experimental work under examination is made up of six main parts:

1. The stage of the control board (three-phase inverter).
2. The second step is the power stage.
3. Design and install a prototype three-to-six-phase transformer with a capacity of 3300 VA and a 220/220 V voltage.
4. A six-phase modified IM with a 3 hp, three-phase IM, prototype 380 V, 2-pole.

Fig. 8 – Block diagram shows the experimental setup at Kafrelshiekh University's Electrical Power Laboratory.

5. Instruments for measuring.
6. A power outage (centrifugal pumping).

9.2. STUDIED CASES

The entire system under study was modeled using the Matlab software to explore the v/f (scalar) control approach. The results have been obtained by using a six-phase IM, tested in the laboratory. As stated in Table 1, eight scenarios have been provided to replicate the various operating situations. Table 2 lists the six-phase IM parameter values. The PID controller is hand-tuned to obtain the desired speed.

Table 1

Eight cases were researched

Period No.	Period (min.) From	To	Description	solar irradiance *G*
1	0	0.59	starting	1
2	0.59	1	normal to 2 900 rpm	1
3	1	1.5	reduce to 2 000 rpm	1-0.6
4	1.5	2	reduce to 1 500 rpm	0.6
5	2	2.5	reduce to 1 000 rpm	0.6
6	2.5	3	Increase to 1 500 rpm	1
7	3	3.5	Increase to 2 000 rpm	0.6
8	3.5	4	Return to to 2 900 rpm	0.6-1

Table 2

Six-phase IM parameter values

Symbol	Value	Symbol	value
V_{ph} [V]	220	*p* (poles)	2
L_{ls} [H]	0.0409	*J* [kgm^2]	0.003
R_s [Ω]	12	L_m [H]	0.849
L_{lr} [H]	0.0409	R_r [Ω]	8.097

9.3 SIMULATION AND EXPERIMENTAL RESULTS

A perovskite PV array consists of 48992 PV modules arranged in groups of 16 series, connected in parallel, each containing 3062 modules. The perovskite solar cells parameters are given in Table 3.

Table 3

Perovskite solar cells; cell, module, and array specifications

	V_{oc} [V]	I_{sc}	I_{pm}	V_{pm} [V]	P_{max} [W]	*A*
Cell	1.05	24.6 mA/cm^2	23.01 mA/cm^2	0.94	0.0216	0.10 cm^2
Module	37.8	0.0049 A	0.00398 A	29.86	0.119	18.00 cm^2
Array	604.8	15 A	13.5 A	478	6453	5.54 m^2

Figures 9–12 illustrate the results of modelling the proposed system to operate a water pump that is driven by solar cells and controlled by a six-phase motor fed by a three-phase drive through conditioner transformer. Figure 9 shows the speed fluctuation with PID (k_i = 0.05, k_p = 0.75, and k_d = 0.005) at deferent speed reference and deferent radiation. We notice from the figure that the motor in the first period accelerates to catch up with the reference speed, in the second region the speed approaches the reference speed with an error rate of no more than 2.9 %, the third period decreases the reference speed to 2 000, followed by the speed of the motor in response time Small and at a time of 1.23 seconds the radiation decreases to 60 %, the fourth period decreases the reference speed to 1500, followed by the motor speed with a constant decrease in sunlight. This is followed by an increase in the motor speed at

a low value of sunlight. The seventh period increases the reference speed to 2 000, followed by an increase in the motor speed with a constant decrease in the sun radiation, and the eighth period increases the reference speed to 2 900, followed by an increase in the motor speed at a high value of the sun.

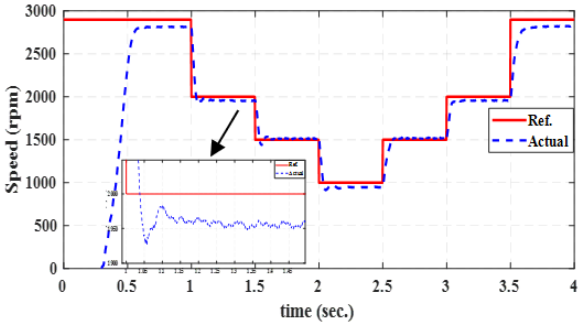

Fig. 9 – Speed time characteristics at different radiation and references.

Figure 10 depicts the performance of the three-phase inverter output voltage after passing through the three-phase to six-phase transformer for the phase voltage of the stator of the six-phase IM for the eight operating periods.

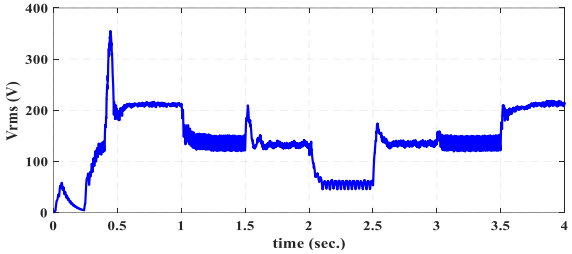

Fig. 10 – Stator phase voltage-time response of six-phase IM.

Figure 11 illustrates that the current stator simulation for the proposed system varies around 1 A and is related to eight operating periods. These graphs illustrate how the procedure reduces the oscillation value, particularly at low speeds, with the mean value falling to its usual value in the second phase.

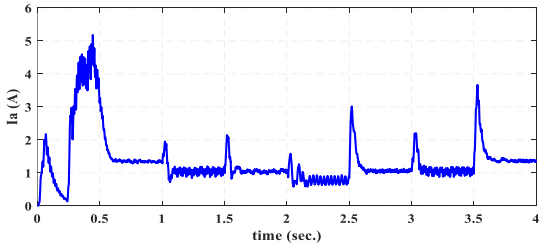

Fig. 11 – Motor stator phase current time response

Figure 12 displays the primary current of a three-to-six-phase transformer that matches the three-phase inverter to the six-phase IM. From Fig. 11 and 12, the current passing through any of the 6 phases in the six-phase IM has been reduced by half, proving one of this motor's features.

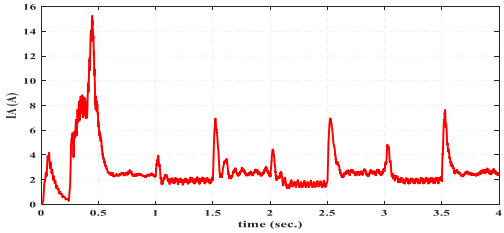

Fig. 12 – Transformer phase current time response.

The statistical analysis ousing perovskite solar cells to operate an induction motor driven by a conditioner transformer fed by a 3-phase inverter through a boost The converter is shown in Table 4 for the steady-state error and oscillation range.

Table 4

Assessment of statistical value for motor rotor speed

Speed (rpm) State	Period	rpm	Period	rpm
steady state error	1	2500	5	945
Oscillation range		0		10
steady state error	2	2815	6	1520
Oscillation range		12.5		15
steady state error	3	1955	7	1558
Oscillation range		12		10
steady state error	4	1510	8	2820
Oscillation range		20		10

Figure 13 displays the torque values for both modeled and experimental loads under standard radiation conditions and a variation in the rotor speed. This graph illustrates that the simulated values are extremely close to the measured values. A convergence between the anticipated practical model ranges and the equivalent mathematical model is demonstrated by the discrepancy between the measured and predicted pump torque values, which range from 3.4 to 15 %.

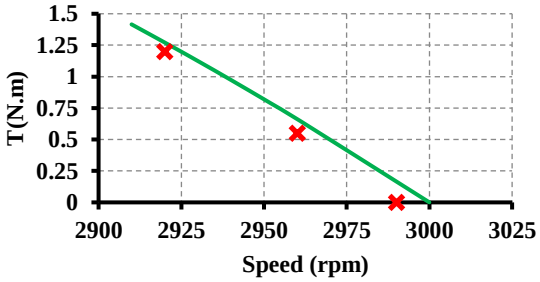

Fig. 13 – Torque-speed characteristics (- simulation, x experimental).

10. CONCLUSIONS

In this work, a genetic algorithm is used to provide MPPT for perovskite solar cells used as a power generation unit in independent mode to feed the six-phase motor to manage the pumping system, which is controlled through a three-phase inverter and an electrical transformer from the three-phase system to the six-phase system. The cost of 1 W in silicon solar cells is almost 70 cents, while in perovskite solar cells, it is almost 10–20 cents, only leading to the proposed system cost reduction. For feeding the six-phase induction motor in this study, a perovskite solar cell array with an area of 1.88 m^2 is needed, while for the same application to feed the induction motor from a silicon-based solar cell array at the same rate of power, an area of 13.89 m^2 is needed. The high-power density of the perovskite solar cell case resulted in a compact area, which saved money and prevented partial shading, which is extremely detrimental to the efficiency of any photovoltaic system. The simulation results of a hand-tuned PID obtained with a v/f control employed for the speed control of a 6-phase IM were reviewed. A modified 6-phase IM supplied and controlled by a 3-phase drive was used in this experiment. This work used a three-phase inverter to convert from three to six phases by driving a 6-phase IM using a conditioner transformer. Experimental and computed mechanical torque levels differ by 3.14 to 15 %, suggesting convergence between the suggested experimental model and the analytical method. As seen in the speed and voltage profiles, our suggested solution improves the quality of the speed profile and phase stator voltage waveform.

Received on 27 March 2023

REFERENCES

1. Y. Kali *et al.*, *Current control of a six-phase induction machine drive based on discrete-time sliding mode with time delay estimation*, Energies, **12**, *1*, pp. 1–17 (2019).
2. H. Patel, V. Agarwal, S. Member, *MATLAB-based modeling to study the effects of partial shading on PV array characteristics*, **23**, *1*, pp. 302–310 (2008).
3. H. Attia, *High performance PV system based on artificial neural network MPPT with PI controller for direct current water pump applications*, Int. J. Power Electron. Drive Syst., **10**, *3*, p. 1329 (2019).
4. A.K. Mishra, B. Singh, *Solar powered water pumping station utilizing improved cuk converter integrating to storage system*, 20th Natl. Power Syst. Conf. NPSC 2018, pp. 1–6 (2018).
5. R. Kumar, B. Singh, *Solar PV powered-sensorless BLDC motor driven water pump*, IET Renew. Power Gener., **13**, *3*, pp. 389–398 (2019).
6. J. Maes *et al*., *Light Absorption coefficient of CsPbBr 3 perovskite nanocrystals*, J. Phys. Chem. Lett., **9**, *11*, pp. 3093–3097 (2018).
7. S.D. Stranks *et al.*, *Electron-hole diffusion lengths exceeding 1 micrometer in an organometal trihalide perovskite absorber*, Science, **342**, *6156*, pp. 341–344 (2013).
8. A. Kojima, K. Teshima, Y. Shirai, T. Miyasaka, *Organometal halide perovskites as visible-light sensitizers for photovoltaic cells*, J. Am. Chem. Soc., **131**, *17*, pp. 6050–6051 (2009).
9. M. Liu, M.B. Johnston, H.J. Snaith, *Efficient planar heterojunction perovskite solar cells by vapour deposition*, Nature, **501**, *7467*, pp. 395–398 (2013).
10. D. Liu *et al.*, *Efficient planar heterojunction perovskite solar cells with Li-doped compact TiO2 layer*, Nano Energy, **31**, pp. 462–468 (2017).
11. A.A. Zaky *et al*., *Enhancing efficiency and decreasing photocatalytic degradation of perovskite solar cells using a hydrophobic copper-modified titania electron transport layer*, Appl. Catal. B Environ., **284**, p. 119714 (May 2021).
12. A.A. Zaky, A. Fathy, H. Rezk, K. Gkini, P. Falaras, A. Abaza, *A modified triple-diode model parameters identification for perovskite solar cells via nature-inspired search optimization algorithms*, Sustainability, **13**, *23*, p. 12969 (2021).
13. A. Messai, A. Mellit, A. Guessoum, S.A. Kalogirou, *Maximum power point tracking using a GA optimized fuzzy logic controller and its FPGA implementation*, Sol. Energy, **85**, *2*, pp. 265–277 (2011).
14. A. Borni *et al.*, *Optimized MPPT controllers using GA for grid connected photovoltaic systems*, *Comparative study*, Energy Procedia, **119**, pp. 278–296 (2017).
15. R.E.-S. Mohamed I. Abdelwanis, *Efficient parameter estimation procedure using sunflower optimization algorithm for six-phase induction motor*, Rev. Roum. Sci. Techn.–Électrotechn. et Énerg, **67**, *3*, pp. 259–264, 2022.
16. M.I. Abdelwanis, R.A. Sehiemy, M.A. Hamida, *Hybrid optimization algorithm for parameter estimation of poly-phase induction motors with experimental verification*, Energy AI, **5**, *100083*, pp. 1–15 (2021),
17. G.C. Seritan, B.A. Enache, F.C. Adochiei, F.C. Argatu, C. Christodoulou, V. Vita *et al*., *Performance evaluation of photovoltaic panels containing cells with different bus bars configurations in partial shading conditions*, Rev. Roum. Sci. Techn.–Électrotechn. et Énerg., **65**, *1*-2, pp. 67–70 (2020).
18. S. Seba, M. Birane, K. Benmouiza, *A comparative analysis of boost converter topologies for photovoltaic systems using mppt and beta methods under partial shading*, Rev. Roum. Sci. Techn.–Électrotechn. et Énerg., **68**, *4*, pp. 375–380 (2023).
19. A. Asadi, M.S. Karimzadeh, X. Liang, M. S. Mahdavi, G B. Gharehpetian, *A novel control approach for a single-inductor multi-input single-output dc–dc boost converter for PV applications*, IEEE Access, **11**, pp. 114753–114764 (2023).
20. L. Fan, X. Ma, *Maximum power point tracking of PEMFC based on hybrid artificial bee colony algorithm with fuzzy control*, Sci. Rep., **12**, *1*, p. 4316 (2022).
21. S.M. Ulaganathan, R. Muniraj, R. Vijayanand, D. Devaraj, *Novel solar photovoltaic emulation for validating the maximum power point algorithm and power converter*, Rev. Roum. Sci. Techn.–Électrotechn. et Énerg, **68**, *4*, pp. 407–412 (2023).
22. S. Chtita *et al*., *A novel hybrid GWO–PSO-based maximum power point tracking for photovoltaic systems operating under partial shading conditions*, Sci. Rep., **12**, *1*, p. 10637 (2022).
23. A.A.S. Mohamed, A. Berzoy, O. Mohammed, *Optimized-fuzzy MPPT controller using GA for stand-alone photovoltaic water pumping system*, IECON Proc. Industrial Electron. Conf., pp. 2213–2218 (2014).
24. M.I. Abdelwanis, R.A. El-Sehiemy, *A fuzzy-based controller of a modified six-phase induction motor driving a pumping system*, Iran. J. Sci. Technol. – Trans. Electr. Eng., 2019.
25. M.I. Abdelwanis, E. M. Rashad, I.B.M. Taha, F.F. Selim, *Implementation and control of six-phase induction motor driven by a three-phase supply*, Energies, **14**, *22*, p. 7798 (2021).
26. H. Heidari *et al*., *A parallel estimation system of stator resistance and rotor speed for active disturbance rejection control of six-phase induction motor*, Energies, **13**, *5* (2020).
27. A.M. Shata, A.S. Abdel-khalik, R.A. Hamdy, M.Z. Mostafa, *Improved mathematical modeling of six phase induction machines based on fractional calculus*, IEEE Access, **9**, *1-1*, pp 53146-53155 (2021).
28. L. Sadiki, S. El Hani, I. Ouachtouk, S. Guedira, *Optimized feed of six phase induction machine using special transformers*, Intl. Conf. on Electrical and Information Techn. (ICEIT), pp. 2020–2022 (2020).
29. K.B. Rathore, V. Yadav, *Experimental analysis of multilevel inverter fed six-phase induction motor for high power applications*, Rev. Roum. Sci. Techn.–Électrotechn. et Énerg., **67**, *4*, pp. 389–394 (2022).
30. M.I. Abdelwanis, F. Selim, *A sensorless six-phase induction motor driving a centrifugal pump system*, 19th International Middle-East Power Systems Conference, MEPCON 2017 (2018).